AD-A233 143

NPS67-90-001CR

NAVAL POSTGRADUATE SCHOOL
Monterey, California

DTIC
ELECTE
MAR 1 3 1991
S D
D

CONTRACTOR REPORT

SECOND-ORDER FAR FIELD COMPUTATIONAL BOUNDARY

CONDITIONS FOR INVISCID DUCT FLOW PROBLEMS

AUGUST VERHOFF
MCDONNELL AIRCRAFT COMPANY
P.O. BOX 516
ST. LOUIS, MISSOURI 63166

MARCH 1990

PREPARED FOR: NAVAL POSTGRADUATE SCHOOL
              MONTEREY, CALIFORNIA 93943-5000

91 3 14 039

Reviewed by:

RAYMOND P. SHREEVE   E. R. WOOD
Professor   Chairman
Department of Aeronautics   Department of Aeronautics
   and Astronautics   and Astronautics

Released by:

G. E. SCHACHER
Dean of Science and Engineering

i

REPORT DOCUMENTATION PAGE

1a. REPORT SECURITY CLASSIFICATION UNCLASSIFIED			1b RESTRICTIVE MARKINGS			
2a. SECURITY CLASSIFICATION AUTHORITY			3 DISTRIBUTION / AVAILABILITY OF REPORT APPROVED FOR PUBLIC RELEASE: DISTRIBUTION IS UNLIMITED			
2b. DECLASSIFICATION / DOWNGRADING SCHEDULE						
4. PERFORMING ORGANIZATION REPORT NUMBER(S) NPS67-90-001CR			5. MONITORING ORGANIZATION REPORT NUMBER(S) NPS67-90-001CR			
6a. NAME OF PERFORMING ORGANIZATION MCDONNELL AIRCRAFT COMPANY		6b OFFICE SYMBOL (If applicable)	7a. NAME OF MONITORING ORGANIZATION NAVAL POSTGRADUATE SCHOOL			
6c. ADDRESS (City, State, and ZIP Code) P.O. BOX 515 ST. LOUIS, MO63166			7b. ADDRESS (City, State, and ZIP Code) MONTEREY, CALIFORNIA 93943-5000			
8a. NAME OF FUNDING / SPONSORING ORGANIZATION NAVAL AIR SYSTEMS COMMAND		8b. OFFICE SYMBOL (If applicable) AIR931E	9. PROCUREMENT INSTRUMENT IDENTIFICATION NUMBER N62271-85-M-0462			

8c. ADDRESS (City, State, and ZIP Code) WASHINGTON, D.C. 20361	10. SOURCE OF FUNDING NUMBERS			
	PROGRAM ELEMENT NO. 61153N	PROJECT NO. WR024	TASK NO 03	WORK UNIT ACCESSION NO. 001

11. TITLE (Include Security Classification)

SECOND-ORDER FAR FIELD COMPUTATIONAL BOUNDARY CONDITIONS FOR INVISCID DUCT FLOW PROBLEMS

12. PERSONAL AUTHOR(S)
VERHOFF, AUGUST

13a. TYPE OF REPORT FINAL	13b TIME COVERED FROM SEP 1985 TO SEP 1988	14. DATE OF REPORT (Year, Month, Day) 1990 MARCH	15. PAGE COUNT 46

16. SUPPLEMENTARY NOTATION

17.	COSATI CODES		18 SUBJECT TERMS (Continue on reverse if necessary and identify by block number)
FIELD	GROUP	SUB-GROUP	COMPUTATIONAL BOUNDARY CONDITIONS
			INTERNAL FLOW COMPUTATIONS
			EULER METHODS

19. ABSTRACT (Continue on reverse if necessary and identify by block number)

HIGHLY ACCURATE FAR FIELD COMPUTATIONAL BOUNDARY CONDITIONS FOR INVISCID, TWO-DIMENSIONAL ISENTROPIC DUCT FLOW PROBLEMS ARE DEVELOPED FROM ANALYTIC SOLUTIONS OF THE LINEARIZED, SECOND-ORDER EULER EQUATIONS. THE EULER EQUATIONS ARE LINEARIZED ABOUT A CONSTANT PRESSURE, RECTILINEAR FLOW CONDITION. THE BOUNDARY PROCEDURE CAN BE USED WITH ANY NUMERICAL EULER SOLUTION METHOD AND ALLOWS COMPUTATIONAL BOUNDARIES TO BE LOCATED EXTREMELY CLOSE TO THE NONLINEAR REGION OF INTEREST. NUMERICAL RESULTS ARE PRESENTED WHICH SHOW THAT THE BOUNDARY CONDITIONS AND FAR FIELD ANALYTIC SOLUTIONS PROVIDE A SMOOTH TRANSITION ACROSS A COMPUTATIONAL BOUNDARY TO THE TRUE FAR FIELD CONDITIONS AT INFINITY. THE COST OF UPGRADING FIRST-ORDER BOUNDARY CONDITIONS TO SECOND-ORDER IS SLIGHT.

20 DISTRIBUTION / AVAILABILITY OF ABSTRACT ☒ UNCLASSIFIED/UNLIMITED ☐ SAME AS RPT ☐ DTIC USERS	21. ABSTRACT SECURITY CLASSIFICATION UNCLASSIFIED	
22a. NAME OF RESPONSIBLE INDIVIDUAL RAYMOND P. SHREEVE	22b TELEPHONE (Include Area Code) (408) 646-2593	22c OFFICE SYMBOL AA/SF

DD FORM 1473, 84 MAR · 83 APR edition may be used until exhausted · All other editions are obsolete

☆ U.S. Government Printing Office: 1986—806-24.

SECOND-ORDER FAR FIELD

COMPUTATIONAL BOUNDARY CONDITIONS

FOR INVISCID DUCT FLOW PROBLEMS

A. Verhoff

McDonnell Aircraft Company
St. Louis, Missouri

March 1990

ABSTRACT

Highly accurate far field computational boundary conditions for inviscid, two-dimensional isentropic duct flow problems are developed from analytic solutions of the linearized, second-order Euler equations. The Euler equations are linearized about a constant pressure, rectilinear flow condition. The boundary procedure can be used with any numerical Euler solution method and allows computational boundaries to be located extremely close to the nonlinear region of interest. Numerical results are presented which show that the boundary conditions and far field analytic solutions provide a smooth transition across a computational boundary to the true far field conditions at infinity. The cost of upgrading first-order boundary conditions to second-order is slight.

I. INTRODUCTION

Numerical solution procedures for nonlinear fluid dynamic equations usually use one or more artificial computational boundaries located at some distance from the primary region of interest in order to limit the physical domain to finite size. If the flow crossing such a boundary (either inflow or outflow) is subsonic, then some type of computational boundary conditions must be imposed which simulate the influence of the true far field conditions at infinity. These boundary conditions must be such that waves crossing the boundary do not produce erroneous reflections back into the computational field to degrade the calculations. It is generally acknowledged that simply imposing free stream conditions (or conditions at infinity) at computational boundaries is usually inappropriate because of the spurious reflections back into the computational domain which result. Standard practice has consisted of locating the boundaries quite far from the region of interest in an attempt to simplify the boundary condition models and minimize any effects of inconsistent modeling. The net effect is a significant increase in the number of grid points required for an accurate flowfield calculation.

A boundary modeling procedure for two-dimensional internal flows was presented in Reference 1 which alleviates the difficulties mentioned above and also allows the computational boundaries to be located much closer to the nonlinear region of interest. The procedure is limited to steady, inviscid flow, although the flow can be rotational. It represents a logical first-order extension of the so-called characteristic (or zero-order) boundary conditions commonly used with inviscid numerical solution methods. Extension to axisymmetric or three-dimensional flows is straightforward.

The analysis presented here extends the first-order analysis to second order for isentropic duct flow and provides a logical extension, in an asymptotic sense, of the first-order analysis. It also illustrates a consistent procedure for coupling linearized analytic solutions with nonlinear numerical solutions by means of computational boundary conditions. The greater accuracy of the second-order boundary procedure allows the computational boundaries to be placed even closer to the nonlinear computational

1

region thereby further reducing the number of grid points needed for the numerical solution. Even though the analysis and boundary conditions derived from it are limited to isentropic flow, many non-isentropic duct flow problems have isentropic flow crossing the inflow boundary at which these second-order boundary conditions can be imposed.

The present analysis is based on the Riemann variable formulation of the Euler equations given in Reference 2 simplified by the isentropic assumption. This represents a natural starting point because the characteristic (or zero-order) boundary conditions mentioned above are expressed in terms of Riemann variables. The equations are linearized about a constant pressure, rectilinear flow condition, which truly represents conditions at infinity. These linearized equations are assumed applicable in the far field region beyond a computational boundary. Within the nonlinear computational domain, strong entropy-producing (i.e., rotational) effects can exist which create variations in density, velocity, etc. in the downstream far field in the streamline-normal direction which are not necessarily small perturbations. Such variations were modeled in the analysis presented in Reference 1. However, because of the two-level perturbation procedure and subsequent approximate solution method used in that analysis, inclusion of entropy effects in the second-order analysis does not seem justified. As mentioned above, however, the second-order isentropic analysis is still applicable to non-isentropic problems having isentropic inflow conditions.

The first-order linearized equations analyzed in Reference 1 are homo-geneous and were solved using separation of variables and Fourier analysis. The second-order equations treated herein are non-homogeneous, but can also be solved by the same techniques. These equations are written in different forms for the upstream and downstream far field regions because the downstream flow is driven by the distribution of flow angle on the computational boundary while the upstream flow is driven by the distribution of Riemann variable associated with upstream propagating waves. The assumption is made that the far field flow is confined by parallel walls, which is not restrictive for duct flow problems.

2

The first- and second-order solutions are coupled to the nonlinear numerical solution to provide a smooth transition across the computational boundary to the true far field conditions at infinity. The coupling is accomplished by the boundary conditions. The first-order boundary conditions provide distributions of flow quantities to be imposed along the boundary, not constant conditions. The second-order boundary conditions provide high accuracy corrections to the first-order distributions. The first- and second-order boundary conditions represent logical asymptotic extensions of the zero-order (or characteristic) conditions. Furthermore, the boundary analysis can be coupled with any inviscid numerical solution method.

Numerical results are presented for a duct/nozzle configuration. Results obtained using the second-order boundary conditions are compared with those using zero- and first-order conditions. An extremely fine grid was used for the numerical solution in order to accurately assess the improvement produced by the second-order analysis. It was found that the computational boundaries could be located very close when the second-order boundary conditions were used with no loss in numerical solution accuracy. The reduced size of the computational field further reduced the number of grid points needed for the numerical solution. The additional computational effort required to upgrade the boundary conditions to second-order is very slight. The benefits of the improved boundary conditions are also achieved when a coarser grid is used.

II. SECOND-ORDER PERTURBATION EQUATIONS

The system of two-dimensional, steady, linearized Euler equations which describe second-order perturbations from a constant pressure state are derived in this section. For reasons outlined in Reference 1, the Riemann variable formulation of Reference 2 will again be used because of its close relationship with characteristic (or zero-order) boundary conditions commonly used in numerical solution of the nonlinear Euler equations. As explained in the previous section, the analysis will be limited to isentropic flow in ducts having parallel walls.

The two-dimensional, isentropic form of the Euler equations is (Reference 2)

$$\frac{\partial Q}{\partial t} + (q + a) \frac{\partial Q}{\partial s} = - qa \frac{\partial \theta}{\partial n} \tag{1}$$

$$\frac{\partial R}{\partial t} + (q - a) \frac{\partial R}{\partial s} = + qa \frac{\partial \theta}{\partial n} \tag{2}$$

$$\frac{\partial \theta}{\partial t} + q \frac{\partial \theta}{\partial s} = - \frac{a^2}{\gamma q} \frac{\partial P}{\partial n} \tag{3}$$

Velocity magnitude and speed of sound are denoted by q and a, respectively, and P is the logarithm of pressure. The Riemann variables Q and R are defined as

$$Q = q + \frac{2}{\gamma-1} a$$
$$\tag{4}$$
$$R = q - \frac{2}{\gamma-1} a$$

The flow angle is θ, time is denoted by t, and local distances along and normal to the streamline direction are denoted by s and n, respectively.

4

For steady flow the analysis can be greatly simplified by defining a new dependent variable

$$T \equiv Q - R \qquad (5)$$

and replacing equations (1) and (2) by

$$(M^2 - 1) \frac{\partial T}{\partial s} + 2 q M \frac{\partial \theta}{\partial n} = 0 \qquad (6)$$

$$a^2 + \frac{\gamma-1}{2} q^2 = 1 \qquad (7)$$

The local Mach number is denoted by M. Equation (6) is obtained by subtracting equations (1) and (2). Equation (7) is obtained by adding equations (1) and (2) and integrating. The constant of integration, which is proportional to stagnation temperature, can be set to unity by proper choice of non-dimensionalizing quantities. The simplified form of the steady Euler equations is then

$$(M^2 - 1) \frac{\partial T}{\partial s} + 2 q M \frac{\partial \theta}{\partial n} = 0 \qquad (8)$$

$$M^2 \frac{\partial \theta}{\partial s} + \frac{2}{\gamma-1} \frac{1}{T} \frac{\partial T}{\partial n} = 0 \qquad (9)$$

$$a^2 + \frac{\gamma-1}{2} q^2 = 1 \qquad (10)$$

In regions of the flowfield where nonlinear effects are weak, the flow can be treated as a perturbation to a constant pressure, rectilinear flow. Such regions occur near and beyond far field computational boundaries. The dependent variables in equations (8) and (9) can then be expanded in asymptotic series

$$T = T_\infty + T_1 + T_2 + \ldots$$

$$\theta = \theta_\infty + \theta_1 + \theta_2 + \ldots \qquad (11)$$

5

The flow direction at infinity is assumed constant and denoted by θ_∞; T_∞ is also constant because the flow is assumed isentropic. The perturbation quantities T_i and θ_i vanish at infinity. For duct flow between parallel walls, the far field flow angle θ_∞ can be assumed zero.

Consistent with the expansions (11), spatial derivatives in equations (8) and (9) can be approximated by

$$\frac{\partial}{\partial s} = \frac{\partial}{\partial x} + \theta_1 \frac{\partial}{\partial y} - \frac{1}{2} \theta_1^2 \frac{\partial}{\partial x} + \theta_2 \frac{\partial}{\partial y} + \ldots$$

$$\frac{\partial}{\partial n} = \frac{\partial}{\partial y} - \theta_1 \frac{\partial}{\partial x} - \frac{1}{2} \theta_1^2 \frac{\partial}{\partial y} - \theta_2 \frac{\partial}{\partial x} + \ldots$$

(12)

where x and y are reference Cartesian coordinates and θ_1 and θ_2 are measured from the x axis which is aligned with the axis of the duct (see Figure 1).

If expansions (11) and (12) are introduced into equations (8) and (9), the resulting first-order perturbed Euler equations are

$$\beta^2 \frac{\partial T_1}{\partial x} - 2 q_\infty M_\infty \frac{\partial \theta_1}{\partial y} = 0 \tag{13}$$

$$2 q_\infty M_\infty \frac{\partial \theta_1}{\partial x} + \frac{\partial T_1}{\partial y} = 0 \tag{14}$$

The second-order equations are

$$\beta^2 \frac{\partial T_2}{\partial x} - 2 q_\infty M_\infty \frac{\partial \theta_2}{\partial y} = - q_\infty \frac{\partial}{\partial x} [M_\infty^3 \theta_1^2$$

$$+ \frac{1}{2q_\infty^2 M_\infty} (1 + \frac{\gamma-1}{4} M_\infty^2 + \frac{\gamma-1}{4} M_\infty^4) T_1^2]$$

(15)

$$2 q_\infty M_\infty \frac{\partial \theta_2}{\partial x} + \frac{\partial T_2}{\partial y} = q_\infty \frac{\partial}{\partial y} [\frac{M_\infty^3}{\beta^2} \theta_1^2 - \frac{1}{2q_\infty^2 M_\infty} (1 + \frac{\gamma-1}{4} M_\infty^2) T_1^2] \tag{16}$$

Velocity and Mach number at infinity are constant and denoted by q_∞ and M_∞, respectively. The parameter β is defined by

$$\beta \equiv \sqrt{1-M_\infty^2} \tag{17}$$

Procedures for calculating far field quantities such as q_∞ and M_∞ are outlined in Reference 1.

Asymptotic expansions of the Riemann variables Q and R can also be defined as

$$Q = Q_\infty + Q_1 + Q_2 + \dots$$

$$R = R_\infty + R_1 + R_2 + \dots \tag{18}$$

Using the definition (5) and the expansion (11) for T, it follows that

$$T_\infty = Q_\infty - R_\infty$$

$$T_1 = Q_1 - R_1 \tag{19}$$

$$T_2 = Q_2 - R_2$$

$$\cdot$$
$$\cdot$$
$$\cdot$$

Introducing the expansions (11) and (18) into the algebraic equation (10) gives the first- and second-order relationships

$$(1+M_\infty) \, Q_1 - (1-M_\infty) \, R_1 = 0 \tag{20}$$

$$(1+M_\infty) \, Q_2 - (1-M_\infty) \, R_2 + \frac{M_\infty}{q_\infty(1+M_\infty)^2} \left(1 + \frac{\gamma-1}{2} M_\infty^2\right) R_1^2 = 0 \tag{21}$$

These relations will be used later in Section IV where the boundary conditions are derived.

Equations (20) and (21) can also be used to express the perturbation equations in different dependent variables. One such form, which will be convenient later in Sections III and IV, uses R_1 and R_2 in place of T_1 and T_2. In terms of these variables, the first-order equations are

$$(1-M_\infty) \frac{\partial R_1}{\partial x} + q_\infty \frac{\partial \theta_1}{\partial y} = 0 \tag{22}$$

$$q_\infty (1+M_\infty) \frac{\partial \theta_1}{\partial x} - \frac{\partial R_1}{\partial y} = 0 \tag{23}$$

The second-order equations are

$$(1-M_\infty) \frac{\partial R_2}{\partial x} + q_\infty \frac{\partial \theta_2}{\partial y} = \frac{1}{2} q_\infty \frac{\partial}{\partial x} [M_\infty^2 \theta_1^2 + \frac{1}{(1+M_\infty)q_\infty^2} (1 + \frac{\gamma-1}{2} M_\infty^3) R_1^2] \tag{24}$$

$$q_\infty (1+M_\infty) \frac{\partial \theta_2}{\partial x} - \frac{\partial R_2}{\partial y} = \frac{1}{2} q_\infty \frac{\partial}{\partial y} [\frac{M_\infty^2}{1-M_\infty} \theta_1^2$$

$$- \frac{1}{(1+M_\infty)^2 q_\infty^2} (1 + 2M_\infty + \frac{\gamma-1}{2} M_\infty^3) R_1^2] \tag{25}$$

The second-order equations using either choice of dependent variables consist of a coupled pair of non-homogeneous equations whose right hand sides (RHS) are functions of the first-order solution variables.

III. SOLUTION OF SECOND-ORDER EQUATIONS

Solutions of the second-order perturbation equations for duct flows are developed in this section. The first-order duct flow analysis of Reference 1 showed that the behavior of the flow in the downstream far field is governed by the distribution of flow angle θ on the downstream computational boundary. This distribution is obtained from the nonlinear numerical solution. Also, the first-order downstream boundary conditions for the computational domain were expressed in terms of the perturbation variable T_1. Therefore, the second-order equations (15) and (16) are appropriate for analyzing the downstream region.

In the upstream far field region, the flow behavior is governed by the distribution of the Riemann variable R on the upstream computational boundary. This distribution is obtained from the nonlinear numerical solution. The first-order upstream boundary conditions for the computational domain were expressed in terms of the perturbation variables θ_1 and Q_1. Therefore, the second-order perturbation equations (21), (24) and (25) are appropriate for analyzing the upstream region.

Downstream Region

The second-order equations (15) and (16) can be combined into the single equation

$$\beta^2 \frac{\partial^2 \theta_2}{\partial x^2} + \frac{\partial^2 \theta_2}{\partial y^2} = \frac{\partial^2}{\partial x \partial y} \left[M_\infty^2 \theta_1^2 + \frac{1}{4 q_\infty^2} \left(1 + \frac{\gamma-1}{2} M_\infty^2 \right) T_1^2 \right] \tag{26}$$

From Reference 1, the solution of the first-order system (13) and (14) for duct flows can be expressed as

9

$$\theta_1 = \sum_1^\infty A_n \sin n\pi y \; e^{-n\pi x/\beta}$$

$$T_1 = \frac{-2q_\infty M_\infty}{\beta} \sum_1^\infty A_n \cos n\pi y \; e^{-n\pi x/\beta}$$

(27)

where A_n represents the Fourier coefficients of the distribution of flow angle θ on the downstream computational boundary located at $x=0$. The width of the duct has been taken as unity. Note that the solution (27) for T_1 does not include a zero-mode term (i.e., A_0) which is related to the mean value of the perturbation $T-T_\infty$ at the boundary. It was pointed out in Reference 1 that such a term is a second-order effect. This will be verified below. Using the first-order solution in the RHS, equation (26) becomes

$$\beta^2 \frac{\partial^2 \theta_2}{\partial x^2} + \frac{\partial^2 \theta_2}{\partial y^2} = \frac{\pi^2 M_\infty^2}{2\beta^3} \sum_1^\infty \sum_1^\infty A_m A_n \left[\left(2 + \frac{\gamma-3}{2} M_\infty^2 \right) (m^2-n^2) \sin(m-n)\pi y \right.$$

(28)

$$\left. + \frac{\gamma+1}{2} M_\infty^2 (m+n)^2 \sin(m+n)\pi y \right] e^{-(m+n)\pi x/\beta}$$

To satisfy the duct wall boundary conditions of zero flow angle, a particular solution of equation (28) must have the form

$$\theta_2 = \frac{\pi^2 M_\infty^2}{2\beta^3} \sum_1^\infty \sum_1^\infty H_{mn}(x) \sin(m\pm n)\pi y$$

(29)

This results in the two component ordinary differential equations (depending on choice of sign) for each value of m and n

$$\beta^2 H_{mn}'' - \pi^2(m+n)^2 H_{mn} = \frac{\gamma+1}{2} M_\infty^2 (m+n)^2 A_m A_n \; e^{-(m+n)\pi x/\beta}$$

(30)

$$\beta^2 H_{mn}'' - \pi^2(m-n)^2 H_{mn} = \left(2 + \frac{\gamma-3}{2} M_\infty^2\right) (m^2-n^2) A_m A_n \; e^{-(m+n)\pi x/\beta}$$

(31)

10

The respective solutions of these equations are

$$H_{mn} = - \frac{\gamma+1}{4} \frac{M_\infty^2}{\pi\beta} (m+n) \, A_m \, A_n \, x \, e^{-(m+n)\pi x/\beta} \qquad (32)$$

$$H_{mn} = \frac{1}{4\pi^2} (2 + \frac{\gamma-3}{2} M_\infty^2) \frac{m^2-n^2}{mn} A_m \, A_n \, e^{-(m+n)\pi x/\beta} \qquad (33)$$

Referring to the first-order solution (27), the solution for θ_1 can be used to exactly represent the computational boundary distribution of flow angle obtained from the nonlinear numerical solution. This requires that θ_2 vanish at x=0. This can be enforced by adding a solution of the homogeneous portion of equation (31) to the solution (33). The full second-order solution for θ in the downstream region is then

$$\theta = \sum_1^\infty A_n \sin n\pi y \, e^{-n\pi x/\beta} + k_1 \, x \sum_1^\infty \sum_1^\infty (m+n) \, A_m \, A_n \, \sin(m+n)\pi y \, e^{-(m+n)\pi x/\beta}$$

$$ \qquad (34)$$

$$+ k_2 \sum_1^\infty \sum_1^\infty \frac{m^2-n^2}{mn} A_m \, A_n \, \sin(m-n)\pi y \, [e^{-(m+n)\pi x/\beta} - e^{-|m-n|\pi x/\beta}]$$

where

$$k_1 \equiv - \frac{\gamma+1}{8} \frac{\pi M_\infty^4}{\beta^4}$$

$$ \qquad (35)$$

$$k_2 \equiv \frac{M_\infty^2}{8\beta^3} (2 + \frac{\gamma-3}{2} M_\infty^2)$$

The solution for T_2 can be obtained from equation (15) using the solution (29) for θ_2 which was determined above. After integrating, the full second-order solution for T in the downstream region is

11

$$T = T_\infty - \frac{2q_\infty M_\infty}{\beta} \sum_1^\infty A_n \cos n\pi y \, e^{-n\pi x/\beta}$$

$$+ K_1 \sum_1^\infty \sum_1^\infty A_m A_n \cos(m+n)\pi y \left[1 + \frac{\pi}{\beta}(m+n)x\right] e^{-(m+n)\pi x/\beta}$$

$$\text{(36)}$$

$$+ K_2 \sum_1^\infty \sum_1^\infty \frac{A_m}{m} \frac{A_n}{n} \cos(m-n)\pi y \left[(m-n)^2 \, e^{-(m+n)\pi x/\beta} - |m^2-n^2| \, e^{-|m-n|\pi x/\beta}\right]$$

$$+ \sum_1^\infty \sum_1^\infty A_m A_n \left[K_3 \cos(m-n)\pi y + K_4 \cos(m+n)\pi y\right] e^{-(m+n)\pi x/\beta}$$

The coefficients are defined by

$$K_1 \equiv \frac{\gamma+1}{4} \frac{q_\infty M_\infty^5}{\beta^4}$$

$$K_2 \equiv \frac{1}{4} \frac{q_\infty M_\infty^3}{\beta^4} \left(2 + \frac{\gamma-3}{2} M_\infty^2\right)$$

$$\text{(37)}$$

$$K_3 \equiv - \frac{q_\infty M_\infty}{\beta^4} \left(1 + \frac{\gamma+1}{4} M_\infty^2 + \frac{\gamma-3}{4} M_\infty^4\right)$$

$$K_4 \equiv - \frac{q_\infty M_\infty}{\beta^4} \left(1 + \frac{\gamma-3}{4} M_\infty^2 + \frac{\gamma+1}{4} M_\infty^4\right)$$

The solution (36) contains longitudinally decaying plane waves corresponding to $m=n$. They are represented by

$$\bar{T}_2 = K_3 \sum_1^\infty A_n^2 \, e^{-2n\pi x/\beta}$$

$$\text{(38)}$$

$$= - \frac{q_\infty M_\infty}{\beta^4} \left(1 + \frac{\gamma+1}{4} M_\infty^2 + \frac{\gamma-3}{4} M_\infty^4\right) \sum_1^\infty A_n^2 \, e^{-2n\pi x/\beta}$$

At $x=0$ the quantity $\bar{T}_2$ represents the mean value of the perturbation $T-T_\infty$ at the boundary.

The second-order equations (24) and (25) can be combined into the single equation

$$\beta^2 \frac{\partial^2 R_2}{\partial x^2} + \frac{\partial^2 R_2}{\partial y^2} = \frac{1}{2} q_\infty \left\{ \frac{\partial^2}{\partial x^2} \left[M_\infty^2 (1+M_\infty) \theta_1^2 + \frac{1}{q_\infty^2} \left(1 + \frac{\gamma-1}{2} M_\infty^3\right) R_1^2 \right] \right.$$

$$\left. - \frac{\partial^2}{\partial y^2} \left[\frac{M_\infty^2}{1-M_\infty} \theta_1^2 - \frac{1}{(1+M_\infty)^2 q_\infty^2} \left(1 + 2M_\infty + \frac{\gamma-1}{2} M_\infty^3\right) R_1^2 \right] \right\} \tag{39}$$

From Reference 1, the solution of the first-order system (22) and (23) can be expressed as

$$R_1 = \sum_1^\infty C_n \cos n\pi y \; e^{n\pi x/\beta}$$

$$\theta_1 = \frac{-\beta}{q_\infty(1+M_\infty)} \sum_1^\infty C_n \sin n\pi y \; e^{n\pi x/\beta} \tag{40}$$

where C_n represents the Fourier coefficients of the distribution of the Riemann variable perturbation $R-R_\infty$ on the upstream computational boundary located at $x=0$. As explained in Reference 1, the mean value of $R-R_\infty$ on the boundary represented by the zero-mode coefficient C_0 is a second-order effect and is not included in the first-order solution (40). Using the first-order solution in the RHS, equation (39) becomes

$$\beta^2 \frac{\partial^2 R_2}{\partial x^2} + \frac{\partial^2 R_2}{\partial y^2} = \frac{\pi^2}{4\beta^2} \; \frac{1}{q_\infty(1+M_\infty)} \left[\left(1 + M_\infty + M_\infty^2 + \frac{\gamma-1}{2} M_\infty^3 + \frac{\gamma-3}{4} M_\infty^4\right) \right.$$

$$\sum_1^\infty \sum_1^\infty C_m C_n (m+n)^2 \cos(m-n)\pi y$$

$$- \left(1 + M_\infty - 3M_\infty^2 + \frac{\gamma-1}{2} M_\infty^3 - \frac{\gamma-3}{2} M_\infty^4\right) \sum_1^\infty \sum_1^\infty C_m C_n (m-n)^2 \cos(m-n)\pi y$$

$$\left. + (\gamma+1) M_\infty^4 \sum_1^\infty \sum_1^\infty C_m C_n (m+n)^2 \cos(m+n)\pi y \right] e^{(m+n)\pi x/\beta} \tag{41}$$

13

Following the solution procedure used for the downstream region, a particular solution of equation (41) must have the form

$$R_2 = \frac{\pi^2}{4\beta^2 q_\infty (1+M_\infty)} \sum_1^\infty \sum_1^\infty G_{mn}(x) \cos(m \pm n)\pi y \qquad (42)$$

This results in the two component ordinary differential equations (depending on choice of sign) for each value of m and n

$$\beta^2 G_{mn}'' - \pi^2 (m+n)^2 G_{mn} = (\gamma+1) M_\infty^4 (m+n)^2 C_m C_n e^{(m+n)\pi x/\beta} \qquad (43)$$

$$\beta^2 G_{mn}'' - \pi^2 (m-n)^2 G_{mn} = [b_1(m+n)^2 + b_2(m-n)^2] C_m C_n e^{(m+n)\pi x/\beta} \qquad (44)$$

The coefficients b_1 and b_2 are defined by

$$b_1 \equiv 1 + M_\infty + M_\infty^2 + \frac{\gamma-1}{2} M_\infty^3 + \frac{\gamma-3}{2} M_\infty^4$$

$$b_2 \equiv - (1 + M_\infty - 3M_\infty^2 + \frac{\gamma-1}{2} M_\infty^3 - \frac{\gamma-3}{2} M_\infty^4) \qquad (45)$$

The respective solutions of these equations are

$$G_{mn} = \frac{\gamma+1}{2} \frac{M_\infty^4}{\pi\beta} (m+n) C_m C_n x \; e^{(m+n)\pi x/\beta} \qquad (46)$$

$$G_{mn} = \frac{1}{4\pi^2} [b_1 (m+n)^2 + b_2 (m-n)^2] \frac{C_m}{m} \frac{C_n}{n} e^{(m+n)\pi x/\beta} \qquad (47)$$

Referring to the first-order solution (40), with the exception of the mean value, the solution for R_1 can be used to exactly represent the computational boundary distribution of $R-R_\infty$ obtained from the nonlinear numerical solution. This requires that all Fourier modes of R_2 except the zero mode vanish at $x=0$. This can be enforced by adding a solution of the homogeneous portion of equation (44). The solution for R_2 in the upstream region is then

14

$$R_2 = K_5 \times \sum_1^\infty \sum_1^\infty (m+n) \, C_m \, C_n \cos(m+n)\pi y \; e^{(m+n)\pi x/\beta} + 4K_6 \sum_1^\infty C_n^2 \, e^{2n\pi x/\beta}$$

$$+ K_6 \sum_{\substack{1 \\ m \neq n}}^\infty \sum_1^\infty \frac{(m+n)^2}{mn} \, C_m \, C_n \cos(m-n)\pi y \; [e^{(m+n)\pi x/\beta} - e^{|m-n|\pi x/\beta}] \qquad (48)$$

$$+ K_7 \sum_1^\infty \sum_1^\infty \frac{(m-n)^2}{mn} \, C_m \, C_n \cos(m-n)\pi y \; [e^{(m+n)\pi x/\beta} - e^{|m-n|\pi x/\beta}]$$

where

$$K_5 \equiv \frac{(\gamma+1)\pi M_\infty^4}{8\beta^3 q_\infty (1+M_\infty)}$$

$$K_6 \equiv \frac{1}{16\beta^2 q_\infty} \left(1 + M_\infty^2 + \frac{\gamma-3}{2} M_\infty^3\right) \qquad (49)$$

$$K_7 \equiv \frac{-1}{16\beta^2 q_\infty (1+M_\infty)} \left(1 + M_\infty - 3M_\infty^2 + \frac{\gamma-1}{2} M_\infty^3 - \frac{\gamma-3}{2} M_\infty^4\right)$$

The corresponding solution for Q_2 can be obtained from the second-order relation (21) as

$$Q_2 = \frac{1-M_\infty}{1+M_\infty} R_2 - \frac{M_\infty}{q_\infty (1+M_\infty)^3} \left(1 + \frac{\gamma-1}{2} M_\infty^2\right) R_1^2 \qquad (50)$$

The solution for θ_2 can be obtained from equation (24) using the solution (48) for R_2 which was determined above. After integrating, the full second-order solution for θ in the upstream region is

15

$$\theta = \frac{-\beta}{q_\infty(1+M_\infty)} \sum_1^\infty C_n \sin n\pi y \; e^{n\pi x/\beta} + k_3 \sum_1^\infty \sum_1^\infty C_m C_n \sin(m+n)\pi y \; e^{(m+n)\pi x/\beta}$$

$$+ k_4 \; x \sum_1^\infty \sum_1^\infty (m+n) \; C_m C_n \sin(m+n)\pi y \; e^{(m+n)\pi x/\beta}$$

(51)

$$+ k_5 \sum_{\substack{1 \\ m\neq n}}^\infty \sum_1^\infty \frac{m+n}{mn} C_m C_n \sin(m-n)\pi y \left[(m+n)\frac{|m-n|}{m-n} \; e^{|m-n|\pi x/\beta} - (m-n) \; e^{(m+n)\pi x/\beta} \right]$$

$$+ k_6 \sum_1^\infty \sum_1^\infty \frac{m-n}{mn} C_m C_n \sin(m-n)\pi y \left[(m+n) \; e^{(m+n)\pi x/\beta} - |m-n| \; e^{|m-n|\pi x/\beta} \right]$$

The coefficients are defined by

$$k_3 \equiv \frac{1}{4\beta q_\infty^2(1+M_\infty)^2} \left[\beta^2 (1 + M_\infty) + \frac{\gamma+1}{2} M_\infty^3 \right]$$

$$k_4 \equiv - \frac{\gamma+1}{8} \frac{\pi M_\infty^4}{\beta^2 q_\infty^2(1+M_\infty)^2}$$

(52)

$$k_5 \equiv \frac{1}{16\beta q_\infty^2(1+M_\infty)} \left(1 + M_\infty^2 + \frac{\gamma-3}{2} M_\infty^3 \right)$$

$$k_6 \equiv \frac{1}{16\beta q_\infty^2(1+M_\infty)^2} \left(1 + M_\infty - 3M_\infty^2 + \frac{\gamma-1}{2} M_\infty^3 - \frac{\gamma-3}{2} M_\infty^4 \right)$$

The solution (48) also contains longitudinally decaying plane waves corresponding to m=n. They are represented by

$$\bar{R}_2 = 4 \; K_6 \sum_1^\infty C_n^2 \; e^{2n\pi x/\beta}$$

(53)

$$= \frac{1}{4\beta^2 q_\infty} \left(1 + M_\infty^2 + \frac{\gamma-3}{2} M_\infty^3 \right) \sum_1^\infty C_n^2 \; e^{2n\pi x/\beta}$$

From equation (50) the corresponding plane waves for Q are

$$\bar{Q}_2 = \frac{1}{4q_\infty(1+M_\infty)^3}(1 - M_\infty + M_\infty^2 - \frac{\gamma-1}{2}M_\infty^3 + \frac{\gamma-3}{2}M_\infty^4)\sum_1^\infty c_n^2 e^{2n\pi x/B} \qquad (54)$$

At x=0 the quantities $\bar{Q}_2$ and $\bar{R}_2$ represent the mean values of the perturbations Q-Q_∞ and R-R_∞ at the boundary, respectively. Note that the mean value of the R perturbation is predicted by the analysis and not determined directly from the numerical solution as are the other Fourier modes.

17

IV. BOUNDARY CONDITIONS DEVELOPMENT

Second-order boundary conditions for duct flows are developed in this section based on the linearized Euler solutions obtained in the previous section. They represent a logical extension of the first-order boundary conditions developed in Reference 1.

Downstream Boundary

The downstream boundary conditions are derived from the definition (5) rewritten as

$$R = Q - T \tag{55}$$

Using the solution (36) for T and applying the relation (55) at the boundary (assumed located at x=0), the distribution of R on the boundary (i.e., the boundary conditions) is calculated according to

$$R_b = Q_{num} - \frac{4}{\gamma-1} a_\infty + \frac{2q_\infty M_\infty}{\beta} \sum_1^\infty A_n \cos n\pi y$$

$$+ (K_1 + K_4) \sum_1^\infty \sum_1^\infty A_m A_n \cos(m+n)\pi y \tag{56}$$

$$+ \sum_1^\infty \sum_1^\infty [K_2 \frac{(m-n)^2 - |m^2-n^2|}{mn} + K_3] A_m A_n \cos(m-n)\pi y$$

The boundary distribution of Q obtained from the nonlinear numerical solution is denoted by Q_{num}. The zero Fourier mode corresponding to m=n in this expression is proportional to the coefficient K_3. It represents the mean value of the R perturbation at the boundary and is clearly a second-order effect.

Upstream Boundary

The upstream boundary conditions are derived by applying the perturbation relation (50) and the solutions (48) and (51) at the boundary (assumed located at x=0). From these relations the distributions of Q and θ on the boundary (i.e., the boundary conditions) are calculated according to

$$Q_b = Q_\infty + \frac{1-M_\infty}{1+M_\infty} \left[\sum_1^\infty C_n \cos n\pi y + 4 K_6 \sum_1^\infty C_n^2 \right]$$
$$- \frac{M_\infty}{q_\infty(1+M_\infty)^3} \left(1 + \frac{\gamma-1}{2} M_\infty^2 \right) \left[\sum_1^\infty C_n \cos n\pi y \right]^2 \tag{57}$$

and

$$\theta_b = \frac{-\beta}{q_\infty(1+M_\infty)} \sum_1^\infty C_n \sin n\pi y + k_3 \sum_1^\infty \sum_1^\infty C_m C_n \sin(m+n)\pi y$$

$$+ k_5 \sum_{\substack{1 \\ m \neq n}}^\infty \sum_1^\infty \frac{m+n}{mn} \left[\frac{|m^2-n^2|}{m-n} -(m-n) \right] C_m C_n \sin(m-n)\pi y \tag{58}$$

$$+ k_6 \sum_1^\infty \sum_1^\infty \frac{m-n}{mn} [m+n - |m-n|] C_m C_n \sin(m-n)\pi y$$

The zero Fourier mode proportional to K_6 in equation (57) is again evident.

V. APPLICATIONS

Numerical solutions of the Euler equations have been calculated for
two-dimensional, isentropic, steady duct/nozzle flow using the second-order
boundary condition procedures developed in the previous section. Second-order
boundary condition results are compared with those produced using the conven-
tional zero-order characteristic boundary conditions and also the first-order
boundary conditions developed in Reference 1.

A solution algorithm was used for the nonlinear Euler equations (1) - (3)
which is based on the method presented in Reference 2. It uses explicit time
integration to relax to steady state conditions. It should be emphasized that
the boundary condition analysis is independent of the choice of inviscid,
nonlinear solution method.

The duct/nozzle geometry is shown schematically in Figure 1. The flow is
characterized by p_∞, the downstream pressure at infinity, which produces a
mass flow per unit area w through the duct. The linearized solutions given by
equations (34), (36), (48), (50) and (51) are assumed valid in the semi-
infinite regions I and III and the computational boundary conditions are
applied at the upstream and downstream boundaries AA and BB of the nonlinear
computational region II.

The actual shape of the duct/nozzle and the computational grid are shown
in Figure 2. The shape is identical to that used for the calculations pre-
sented in Reference 1. The nozzle contour is sinusoidal and symmetric about
the centerline. The computational grid for this portion of the nozzle had
dimensions 81 x 41, which is twice the size of that used in Reference 1. The
increased grid dimensions allowed second-order effects to be quantified more
accurately. The area ratio of the nozzle is .75 and the upstream and down-
stream areas are equal. For these constant area sections of the duct, addi-
tional rectangular grid cells could be added without altering the basic 81 x
41 grid. This served to minimize the effect of grid changes on the calcula-
tions when the computational boundaries were moved in order to assess the
accuracy of the boundary conditions.

20

Because the configuration is symmetric, calculations were limited to the lower half of the duct and a centerline symmetry condition was used. Although the configuration used for these calculations is simple, the boundary condition analysis of the previous section is general and applicable to unsymmetric configurations having unequal upstream and downstream areas. Use of the simple configuration is sufficient to demonstrate the validity of the analysis.

The second-order upstream and downstream boundary conditions are given by equations (56), (57) and (58). The associated analytic far field solutions are given by equations (21), (34) and (36) for the downstream region and by equations (48), (50) and (51) for the upsteam region. The zero-order (or characteristic) boundary conditions consist of imposing the constant value of Q_∞ and a zero value of θ along the upstream boundary and the constant value of R_∞ along the downstream boundary. The first-order upstream boundary conditions consist of imposing additional distributions of Q_1 and θ_1 along the boundary as determined from equations (20) and (40). The first-order downstream boundary conditions consist of imposing an additional distribution of R_1 along the boundary as determined from equations (27) and (55). Additional details are given in Reference 1.

Computational results are presented for a single value of p_∞, but with the computational boundaries located at two different longitudinal stations. One boundary is sufficiently far removed so that all three sets of boundary conditions produced essentially the same results within the computational domain. The second boundary is extremely close to the nozzle portion of the duct so that the relative accuracy of the various boundary conditions can then be evaluated.

Results obtained using the complete grid shown in Figure 2 are presented in Figures 3 and 4. This grid has 40 columns of grid cells in both the upstream and downstream constant area portions of the duct. As mentioned above the results were nearly identical for all three sets of boundary conditions. Figure 3 shows pressure and Mach number distributions along the centerline and lower wall of the duct/nozzle. Pressure, Mach number, and flow angle contours are presented in Figure 4. These results serve as a reference

for evaluating the accuracy of solutions where the computational boundaries are moved closer to the nozzle portion of the duct.

Results for the shortened computational domain obtained using the zero-order boundary conditions are presented in Figures 5 and 6. There was only one column of grid cells in both the upstream and downstream constant area portions of the duct for this case. Pressure and Mach number distributions are shown in Figure 5 and contours are shown in Figure 6. The degradation in the solution as a result of the boundary proximity is very evident.

Application of the first-order boundary conditions to the short computational domain gives the results shown in Figures 7 and 8. Eleven Fourier modes were needed to accurately describe the boundary distributions of θ and R for this extremely close boundary location. Pressure and Mach number distributions are shown in Figure 7 and contours in Figure 8. Linearized first-order solution results obtained from equations (20), (27) and (40) have been added upstream and downstream of the computational boundaries. Significant improvement is provided by the first-order boundary conditions. Some mismatch at the boundary is evident, but this can be attributed to neglect of second-order interactions.

Finally, results for the shortened computational domain using the second-order boundary conditions are presented in Figures 9 and 10. Eleven Fourier modes were also used in obtaining these results. Pressure and Mach number distributions are shown in Figure 9 and contours in Figure 10. The results within the numerical solution portion of the domain are nearly identical to those shown in Figures 3 and 4. Linearized second-order solution results obtained from equations (48), (50) and (51) and from equations (21), (34) and (36) have been added upstream and downstream of the computational boundaries, respectively. It is evident that the linearized far field analytic solutions provide for a smooth transition across the computational boundary to the true far field conditions at infinity.

A more quantitative comparison between the three sets of boundary conditions can be obtained by examining the distribution of flow variables along the computational boundaries. Figure 11 shows a comparison of the distribu-

22

tion of pressure and flow angle along the upstream and downstream boundaries for the short computational domain. Results at the same longitudinal locations taken from the reference numerical solution using the long grid (Figure 3) are also shown. These results exhibit classical asymptotic convergence to the reference solution. The larger increment between the zero-order and first-order pressure results at the upstream boundary is primarily due to the fact that the zero-order boundary conditions impose a zero flow angle along the boundary.

It was pointed out in Section III and also in Reference 1 that the mean values of the perturbations at the computational boundaries are neglected within the first-order analysis. In Section III they were shown to appear as second-order effects described by equations (38) and (53) evaluated at $x=0$. In the downstream region equation (38) indicates that the relationship

$$[\sum_{1}^{\infty} A_n^2]^{-1} \int_0^1 (T-T_\infty) \, dy = - \frac{q_\infty M_\infty}{\beta^4} (1 + \frac{\gamma+1}{4} M_\infty^2 + \frac{\gamma-3}{4} M_\infty^4) \tag{59}$$

should hold. Likewise, from equation (53) the corresponding relation for the upsteam region is

$$[\sum_{1}^{\infty} C_n^2]^{-1} \int_0^1 (R-R_\infty) \, dy = \frac{1}{4\beta^2 q_\infty} (1 + M_\infty^2 + \frac{\gamma-3}{2} M_\infty^3) \tag{60}$$

These relations are shown in Figure 12 for $p_\infty = 0.90$. The Fourier coefficients and integrals are determined at various longitudinal upstream and downstream locations using flowfield data taken from the reference long grid solution of Figure 3. Distance measured from the start of the constant area portions of the duct is denoted by ξ. These results confirm the second-order nature of the perturbation mean values.

It can be seen from equations (56), (57) and (58) that very little additional computational effort is required to upgrade the boundary conditions from first-order to second-order. Most of the computational effort at the boundaries is spent determining the Fourier coefficients which are needed to impose first-order boundary conditions. Therefore, computational boundaries having isentropic inflow can be upgraded easily even though a source of entropy production may exist within the nonlinear computational domain.

The results presented in Figures 3 through 12 were obtained using a very fine computational grid in order to accurately quantify the differences between the boundary condition models. To demonstrate that the improvement provided by the second-order procedure can also be achieved with a moderately sized grid, the calculations were repeated with the grid used in Reference 1. One column of grid cells was used in both the upstream and downstream constant area portions of the duct. These results are shown in Figures 13 and 14. Pressure and Mach number distributions are shown in Figure 13. Distributions of pressure and flow angle along the upstream and downstream computational boundaries are compared in Figure 14. Note that these boundaries are located slightly upstream and downstream, respectively, from those of the fine grid solution. Asymptotic convergence to the reference solution (Reference 1) is again evident. Eleven Fourier modes were needed to resolve the boundary distributions of θ and R.

VI. SUMMARY

Highly accurate second-order far field boundary conditions for two-dimensional, isentropic duct flow have been developed from analytic solutions of the second-order linearized Euler equations. These boundary conditions represent a logical extension, in an asymptotic sense, of the first-order boundary conditions derived in Reference 1 from analytic solutions of the first-order linearized Euler equations. The first-order boundary conditions of Reference 1 are themselves a logical extension of the zero-order (or characteristic) boundary conditions commonly used in numerical solutions of the nonlinear fluid dynamic equations. The boundary conditions and analytic solutions provide a smooth transition across a computational boundary to the true far field conditions at infinity. The boundary procedure is general in that it can be used in conjunction with any numerical solution method.

The second-order linearized Euler equations are non-homogeneous and have been solved exactly using separation of variables and Fourier analysis. This procedure was used in Reference 1 to solve the linearized, homogeneous first-order equations. Extension of the second-order analysis to allow non-isentropic flow conditions is probably not justified because solution of the non-isentropic equations requires an approximate two-level perturbation procedure (see Reference 1 for details). However, even if the flow being analyzed has an entropy source in the nonlinear region, the second-order boundary conditions can still be applied at the inflow computational boundary if the incoming flow is isentropic.

Use of zero-order (or characteristic) boundary conditions requires that the computational boundaries be located far from the nonlinear region of the flow. Closer placement of the boundaries may result in a significant amount of solution degradation. The first-order boundary conditions derived in Reference 1 allow the boundaries to be located much closer thereby reducing the number of grid points needed for the numerical solution and also the number of iterations for solution convergence. This leads to a significant reduction in the amount of computational effort required for the nonlinear

numerical solution because the additional calculations required for the first-order boundary conditions is modest.

Use of the second-order boundary conditions allows the computational boundary to be placed even closer with a further reduction in the number of grid points. The amount of additional computational and implementation effort is very slight so that isentropic inflow boundary conditions can be upgraded with little penalty.

In Reference 1 it was pointed out that the mean values of the flow variable perturbations at the computational boundary were not described within the first-order analysis. It was further postulated that these mean values represented a second-order effect. The nature of this second-order interaction was clarified by the present analysis and verified by numerical results.

VII. <u>REFERENCES</u>

1. Verhoff, A., "Far Field Computational Boundary Conditions for Internal Flow Problems," Naval Postgraduate School Report, NPS 67-88-001 CR, Sept. 1988.

2. Verhoff, A. and O'Neil, P. J., "A Natural Formulation for Numerical Solution of the Euler Equations," AIAA Paper No. 84-0163, Jan. 1984.
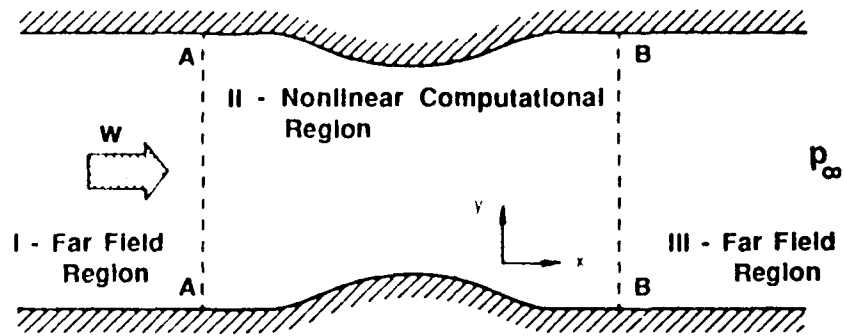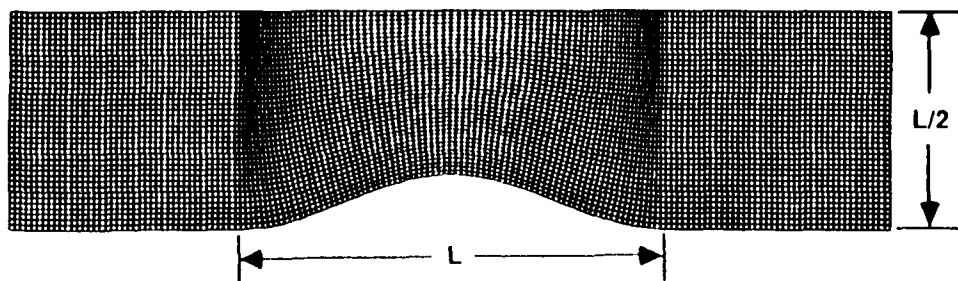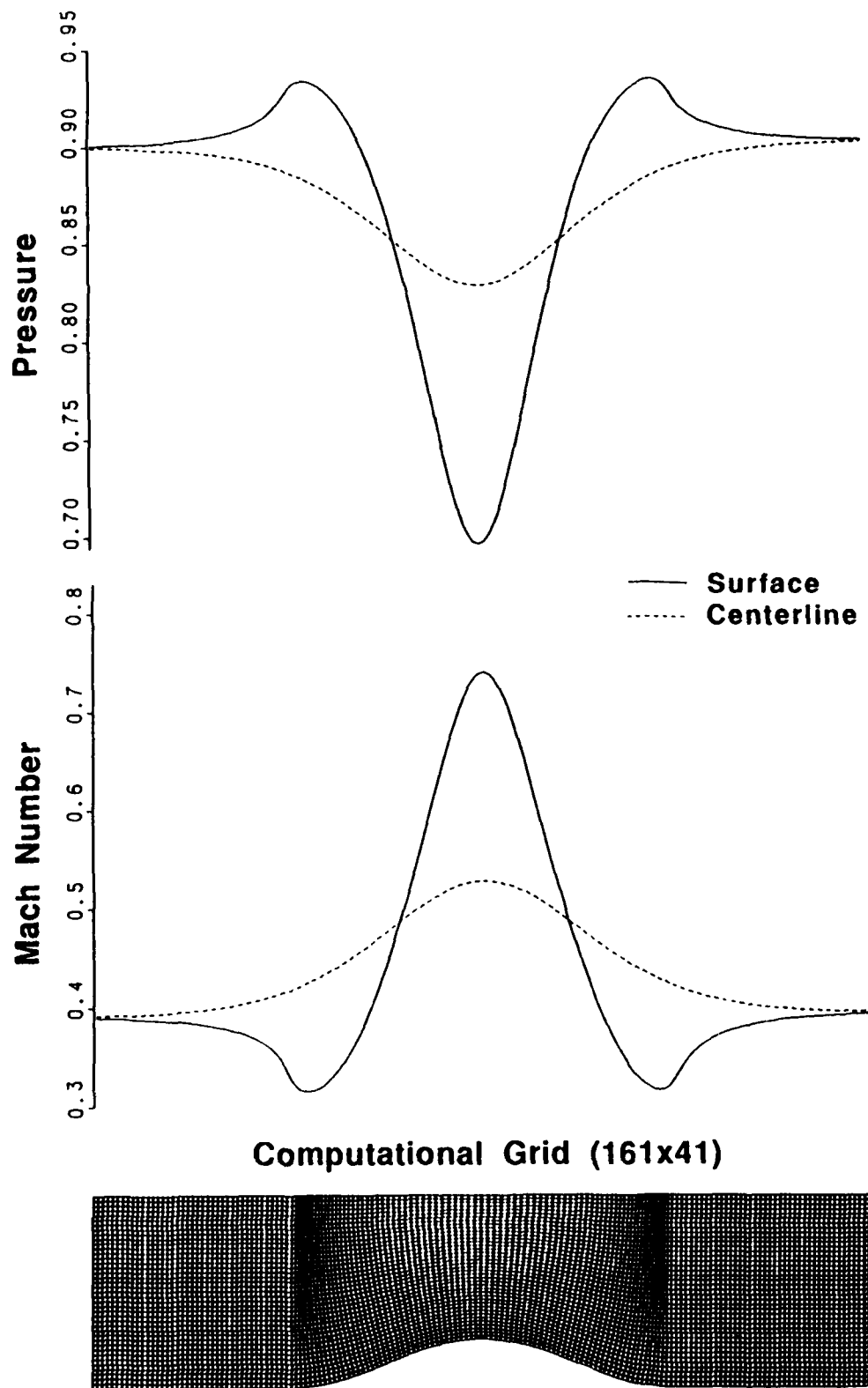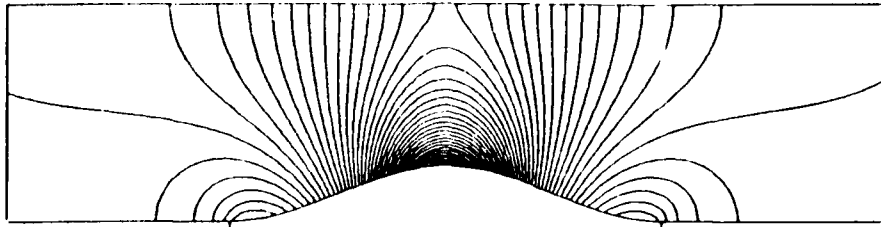
Figure 1. Duct/Nozzle Schematic

Figure 2. Duct/Nozzle Geometry and Grid

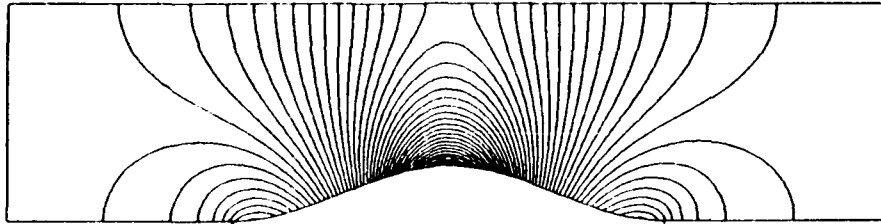**Figure 3. Pressure and Mach Number Distributions**
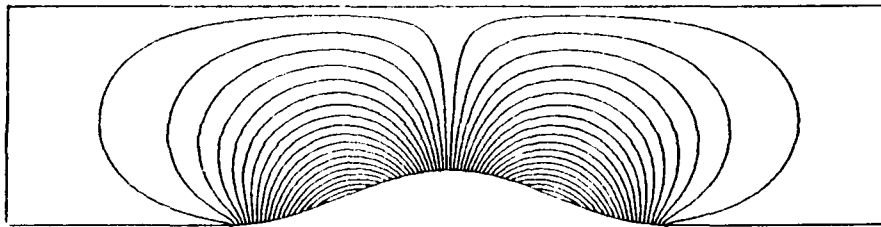**Zero-, First- and Second-Order Boundary Conditions**
$p_\infty = 0.9$
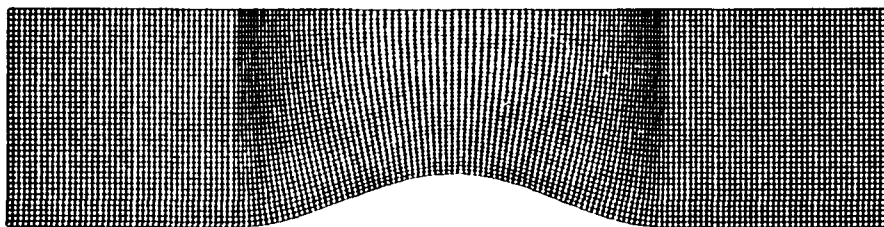
29

Pressure Contours

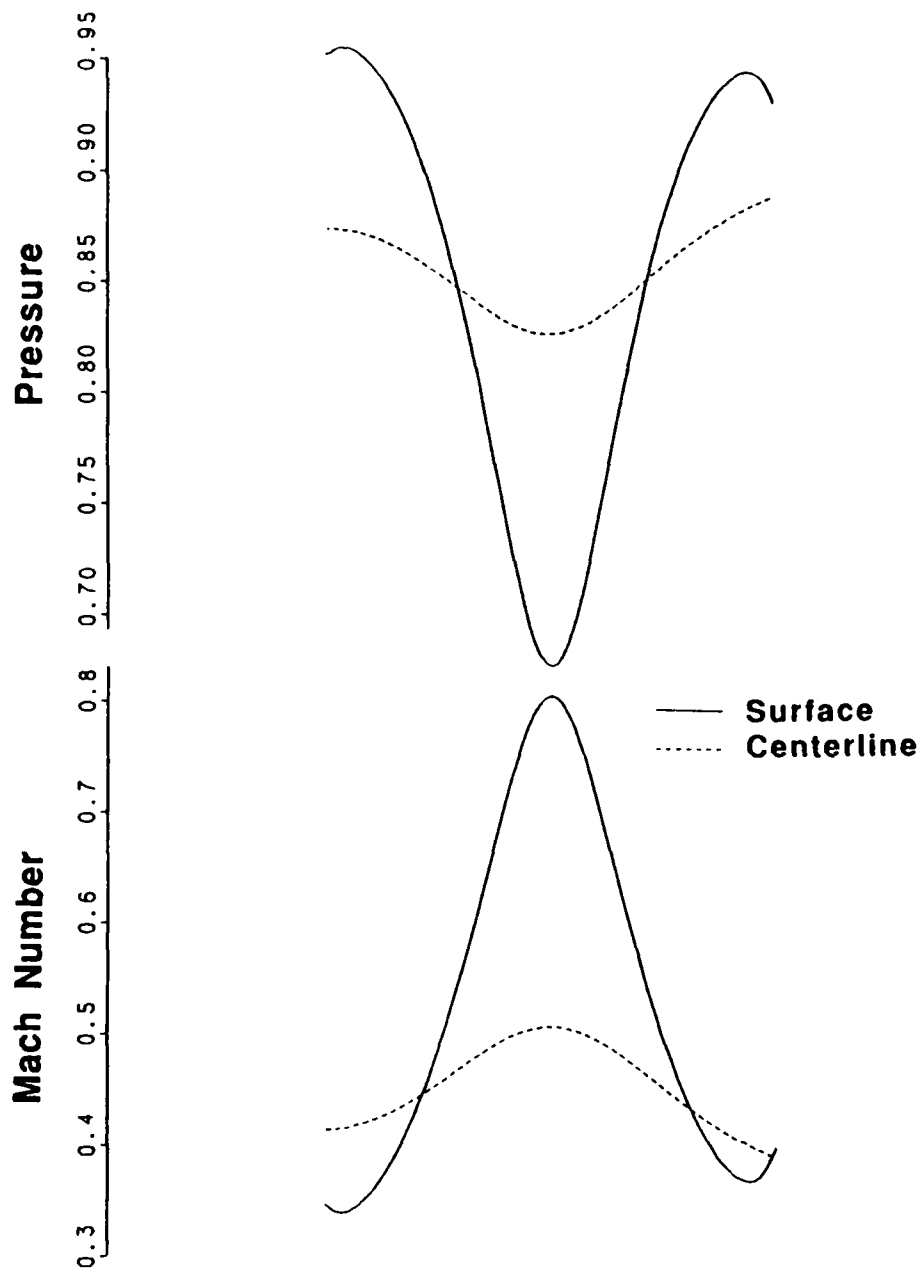**Mach Number Contours**
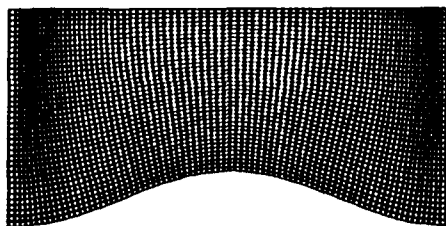

Flow Angle Contours

Computational Grid (161x41)

**Figure 4.   Pressure, Mach Number and Flow Angle Contours
Zero-, First- and Second-Order Boundary Conditions
$p_\infty = 0.9$**

**Figure 5. Pressure and Mach Number Distributions
Zero-Order Boundary Conditions
$p_\infty = 0.9$**

Pressure Contours

Mach Number Contours

Flow Angle Contours

Computational Grid (83x41)

**Figure 6. Pressure, Mach Number and Flow Angle Contours
Zero-Order Boundary Conditions
$p_\infty = 0.9$**
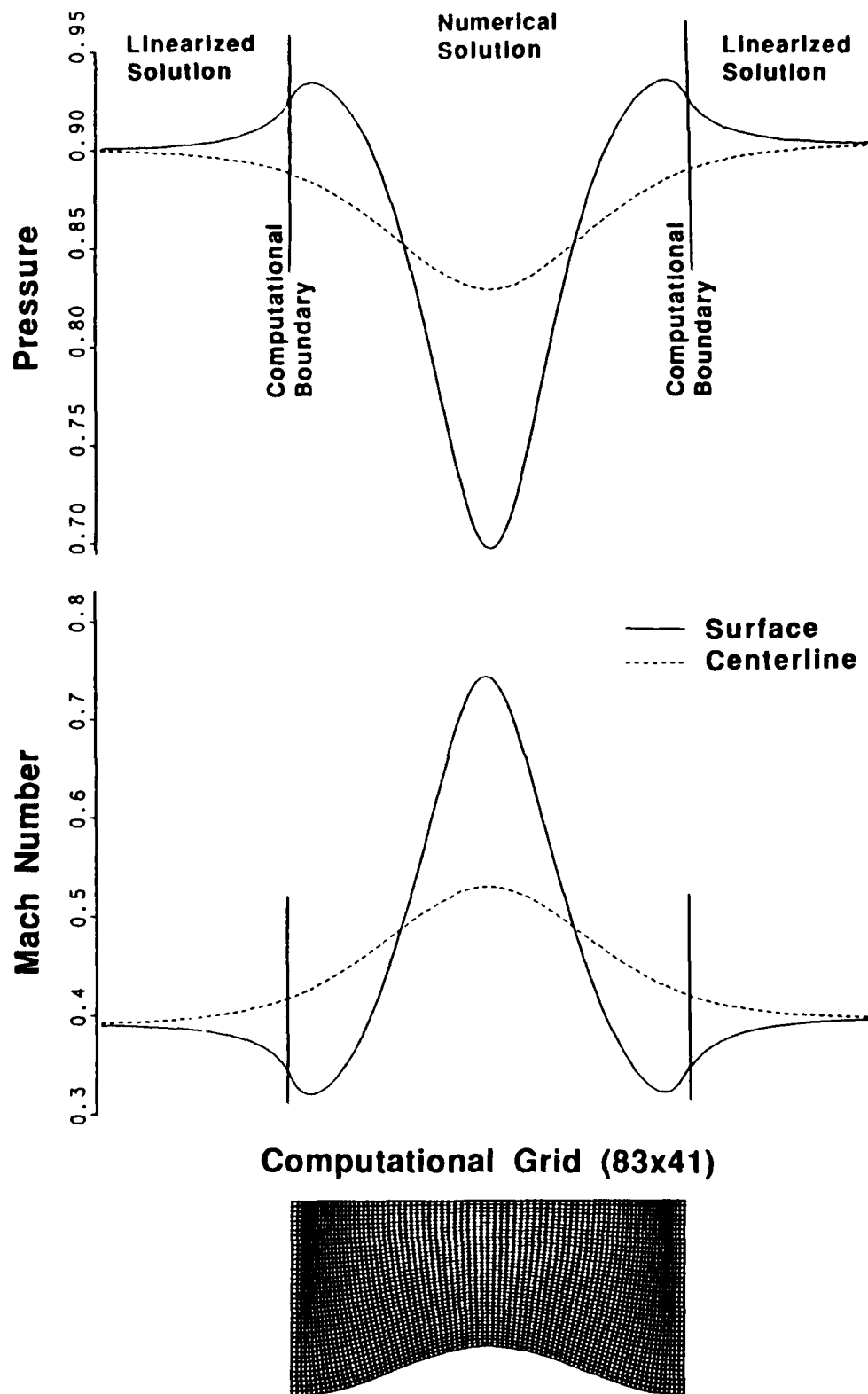
Figure 7. Pressure and Mach Number Distributions
First-Order Boundary Conditions
$p_\infty = 0.9$
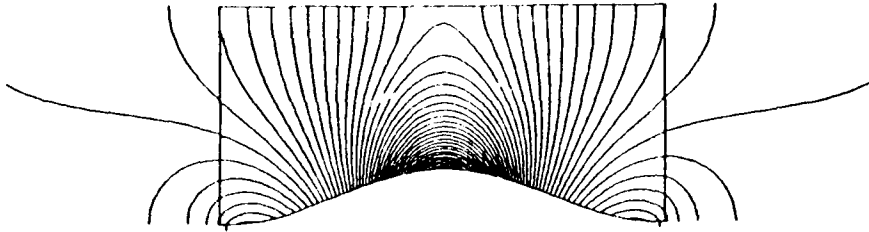
Pressure Contours

Mach Number Contours
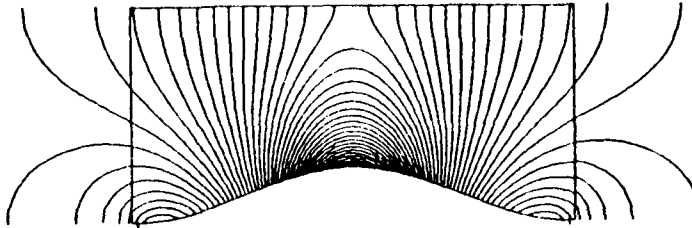
Flow Angle Contours
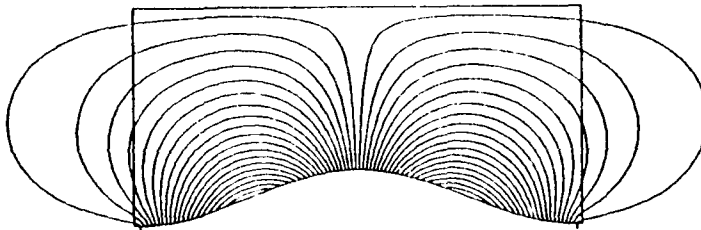
Computational Grid (83x41)
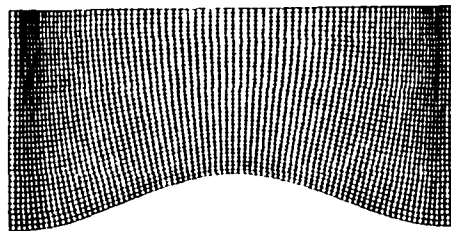
**Figure 8. Pressure, Mach Number and Flow Angle Contours
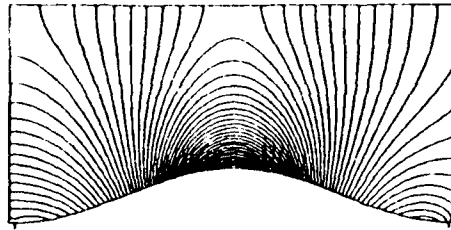First-Order Boundary Conditions
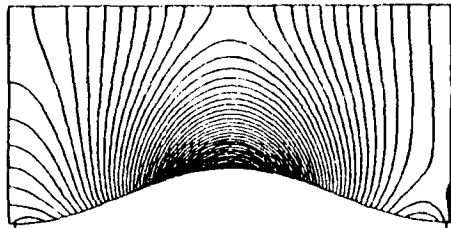$p_\infty \approx 0.9$**

34
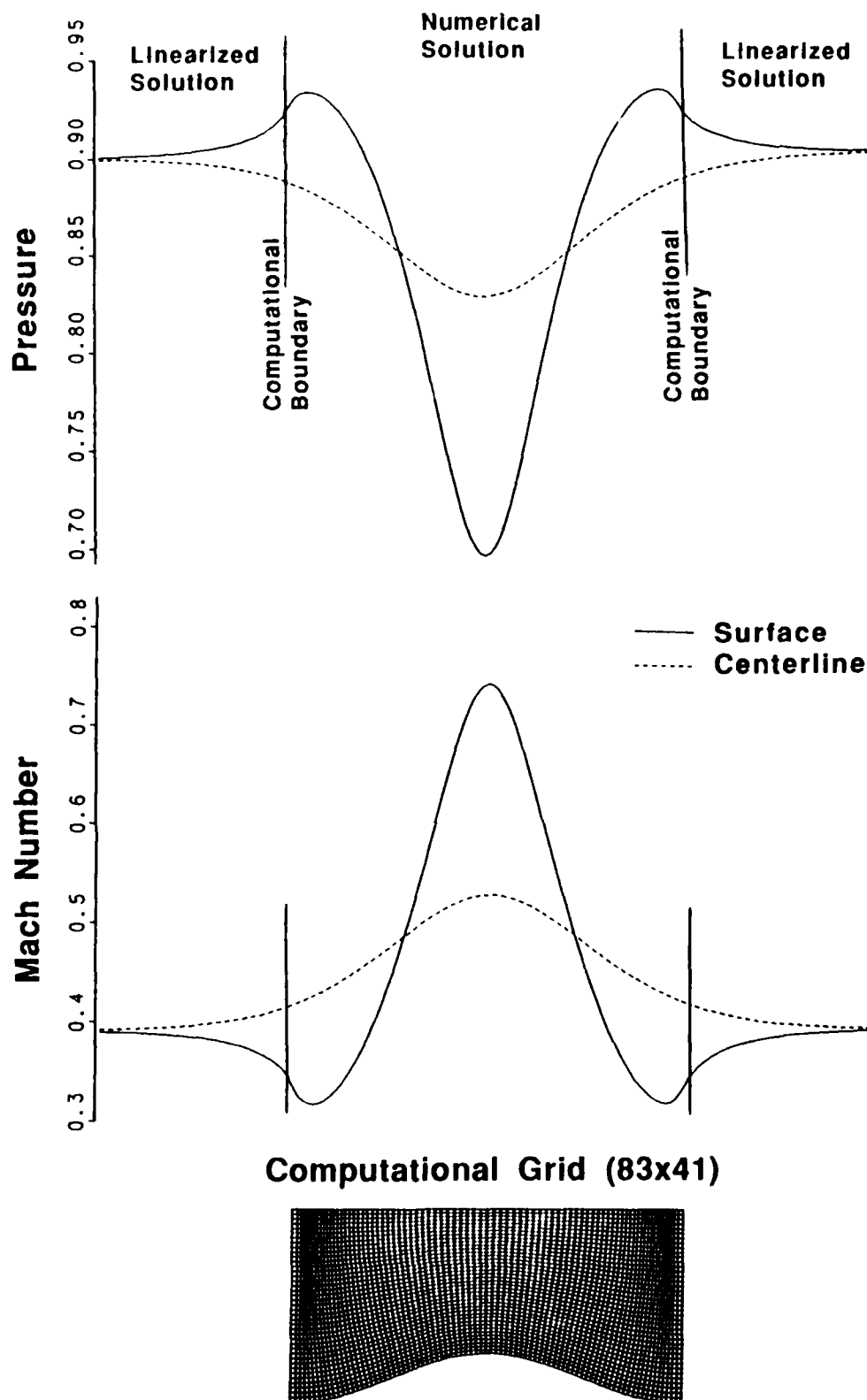
**Figure 9. Pressure and Mach Number Distributions
Second-Order Boundary Conditions
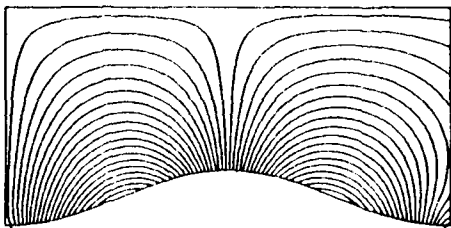$p_\infty = 0.9$**

35
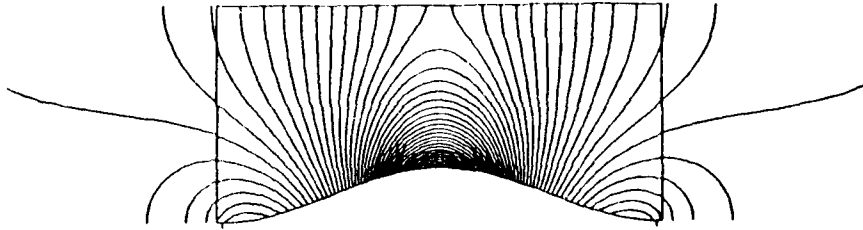
Pressure Contours

Mach Number Contours
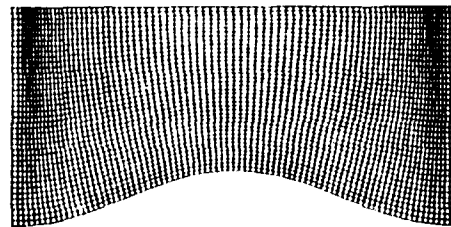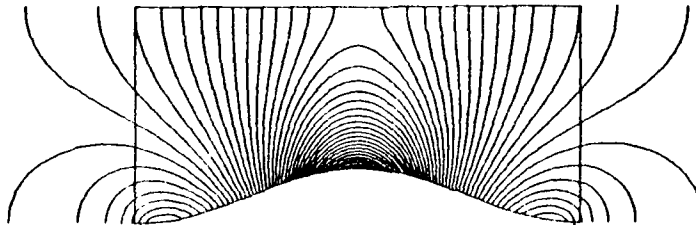

Flow Angle Contours
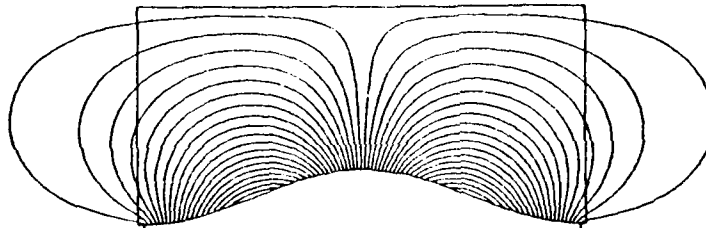
Computational Grid (83x41)
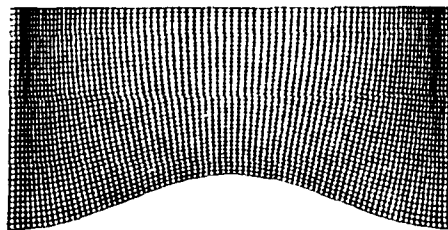
**Figure 10. Pressure, Mach Number and Flow Angle Contours
Second-Order Boundary Conditions
$p_\infty = 0.9$**

36

Pressure Distribution

- ○ Reference Solution
- – – – Zero-Order Boundary Conditions
- ········ First-Order Boundary Conditions
- —— Second-Order Boundary Conditions
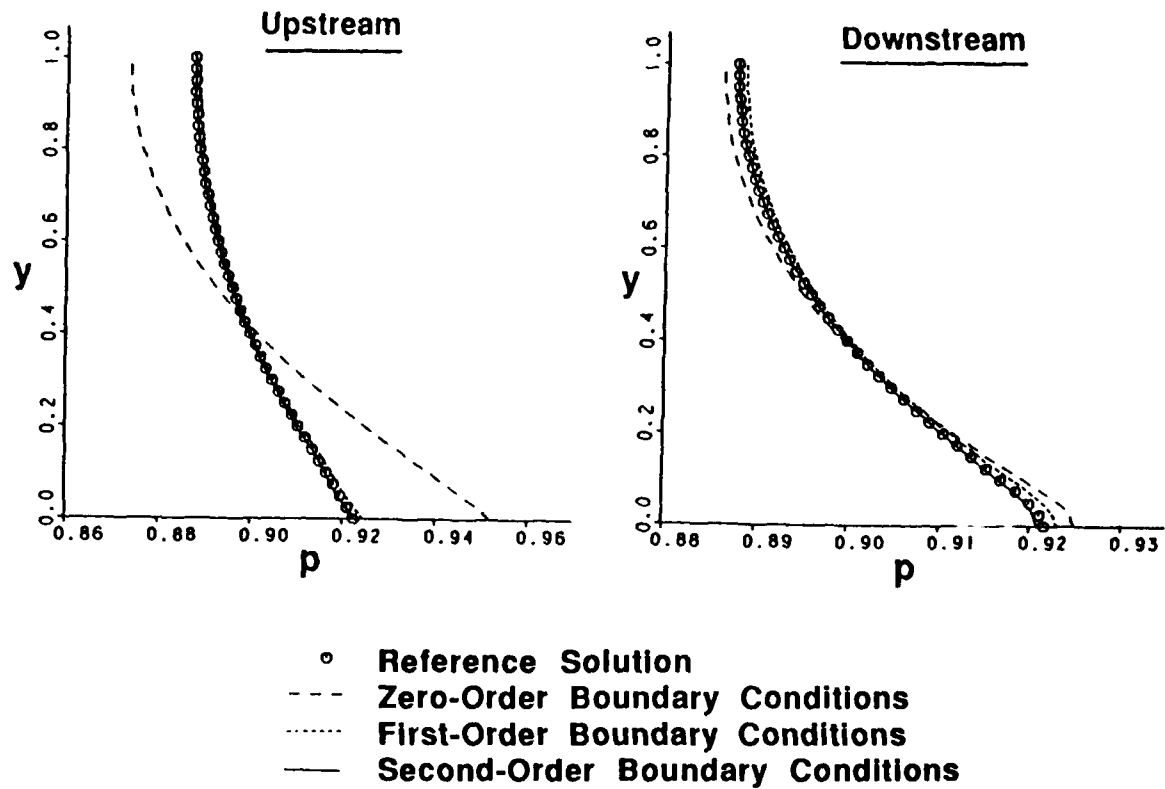
Flow Angle Distribution
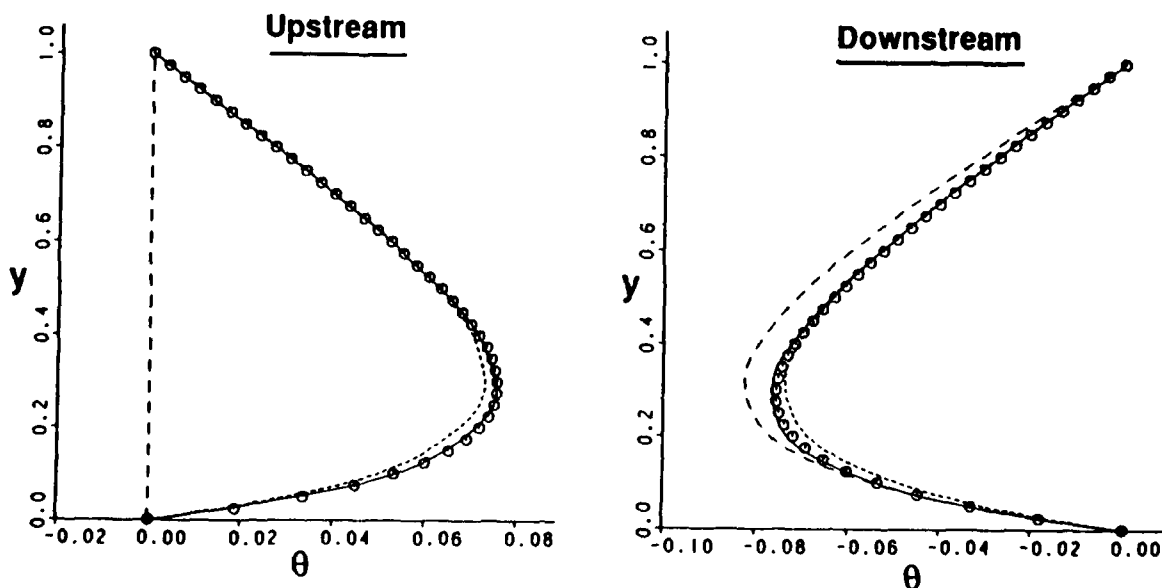
Figure 11. Pressure and Flow Angle Distributions on Computational Boundaries
$$p_\infty = 0.9$$

Upstream

$$\frac{\int_0^1 (R-R_\infty)\, dy}{\sum_1^\infty C_n^2}$$

Downstream

Numerical
------ Theoretical

Equation (59)

$$\frac{1}{4\beta^2 q_\infty}\left(1 + M_\infty^2 + \frac{\gamma-3}{2} M_\infty^3\right)$$

$$\frac{\int_0^1 (T-T_\infty)\, dy}{\sum_1^\infty A_n^2}$$

Equation (60)

$$-\frac{q_\infty M_\infty}{\beta^4}\left(1 + \frac{\gamma+1}{4} M_\infty^2 + \frac{\gamma-3}{4} M_\infty^4\right)$$

-0.4 -0.3 -0.2 -0.1 0.0

ξ

0.0 0.1 0.2 0.3 0.4

ξ
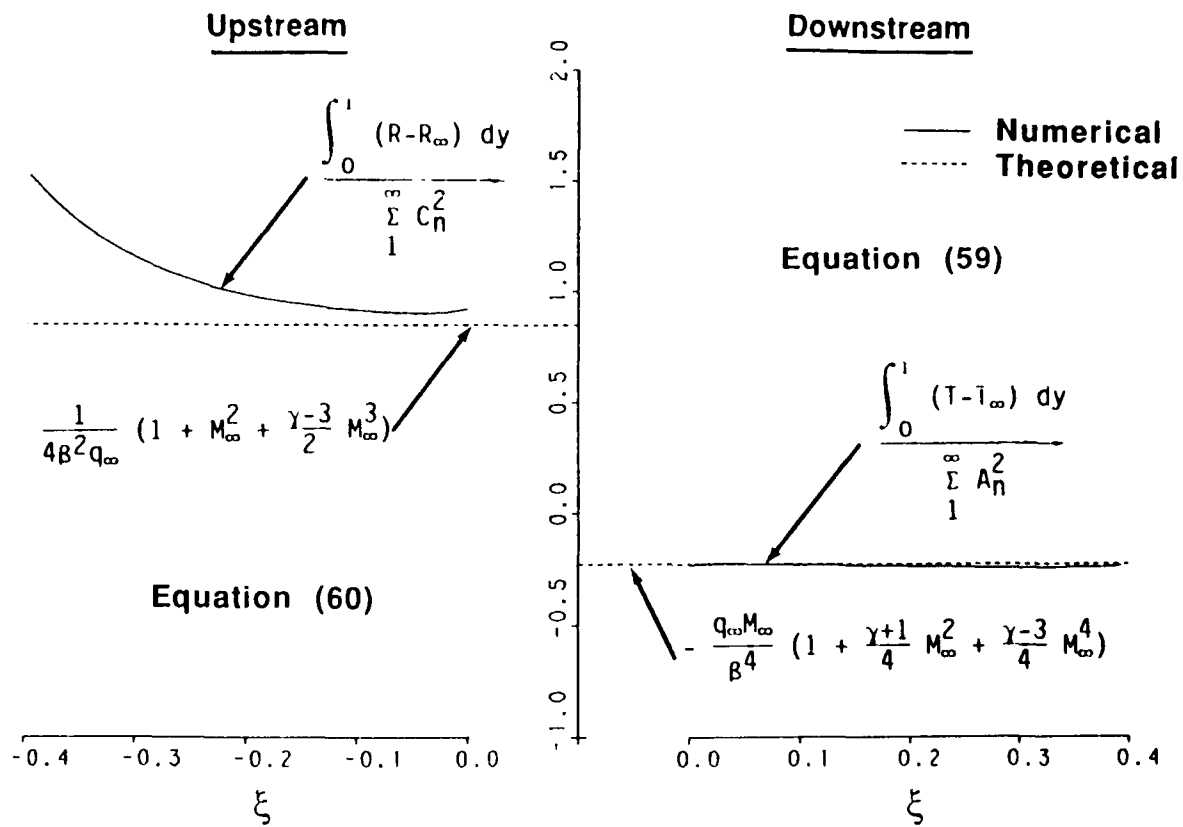
Figure 12. Comparison of Numerical and Theoretical
Perturbation Mean Values
$p_\infty = 0.9$
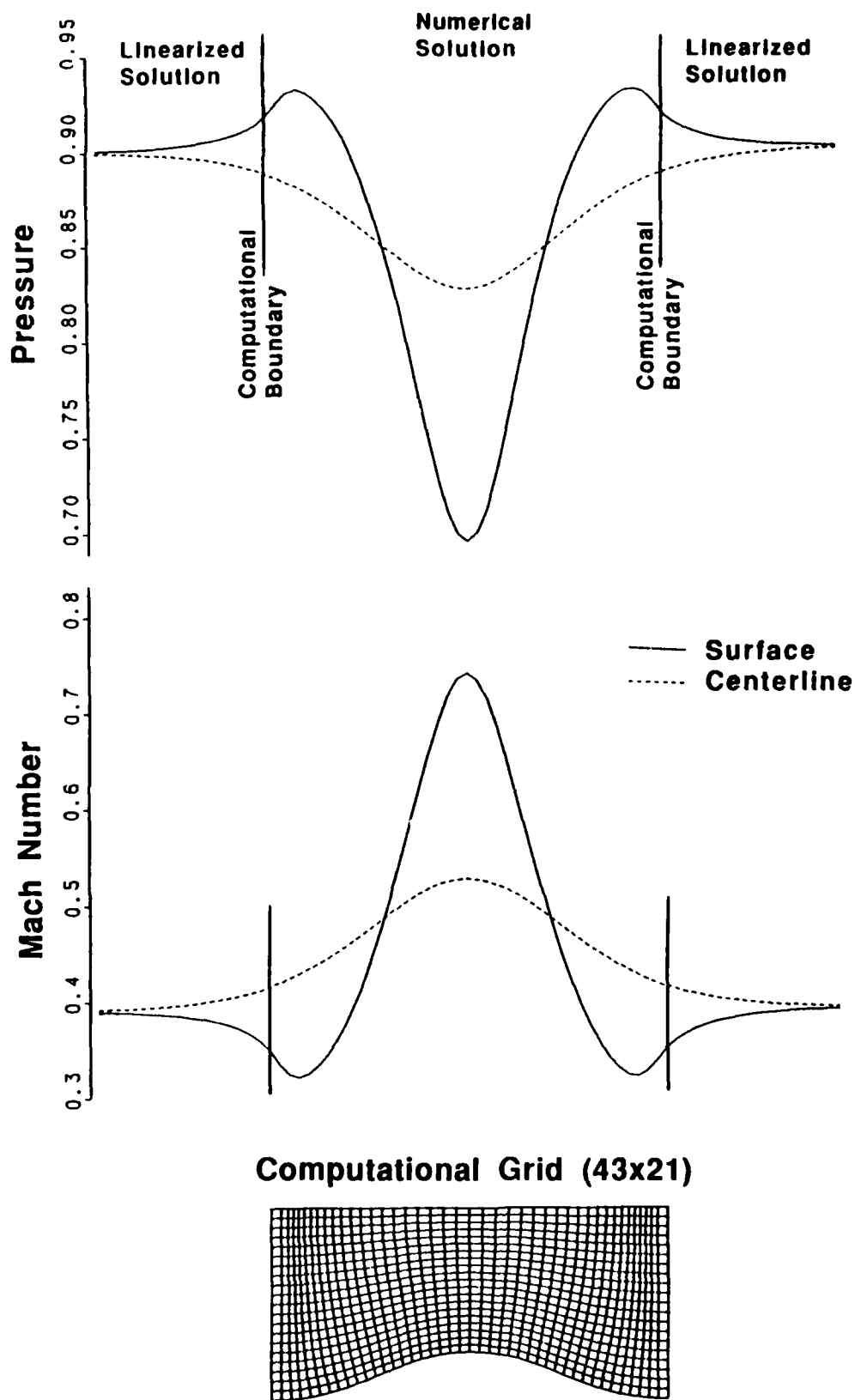
Figure 13. Pressure and Mach Number Distributions
Second-Order Boundary Conditions
$p_\infty = 0.9$

39

Pressure Distribution

Upstream

Downstream

○ Reference Solution
- - - Zero-Order Boundary Conditions
······ First-Order Boundary Conditions
——— Second-Order Boundary Conditions

Flow Angle Distribution

Upstream

Downstream
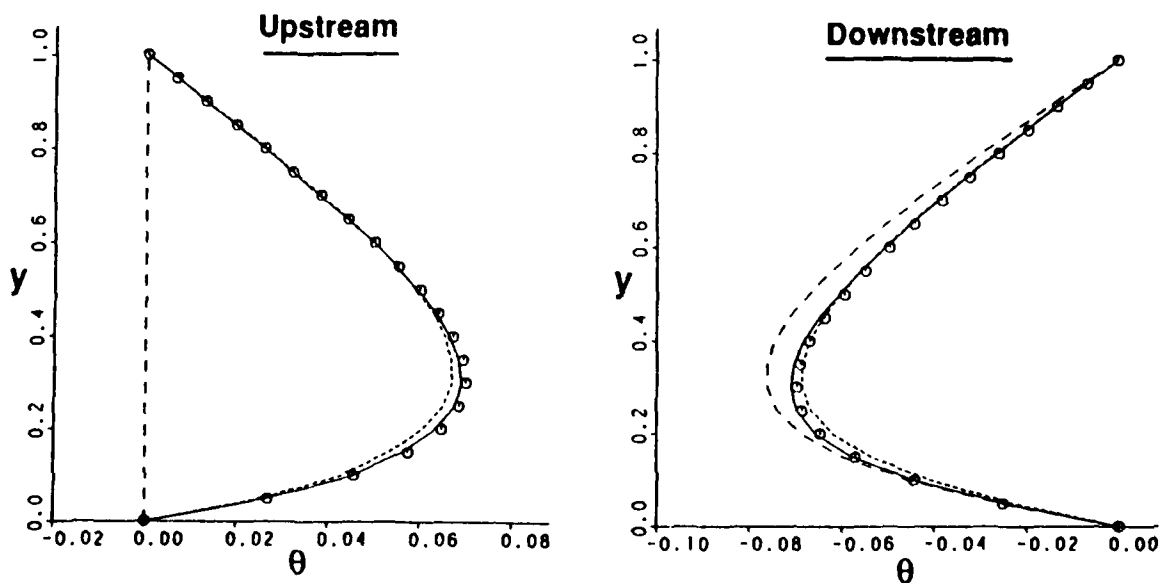
**Figure 14. Pressure and Flow Angle Distributions
on Computational Boundaries
$p_\infty = 0.9$**

40

INITIAL DISTRIBUTION LIST

1. Commander
    Naval Air Systems Command
    Washington, DC 20361
    Attention: Code AIR 931   1
                Code AIR 931E   1
                Code AIR 530   1
                Code AIR 536   1
                Code AIR 5004   4
                Code AIR 93D   1

2. Office of Naval Research
    800 N. Quincy Street
    Arlington, VA 22217
    Attention: Dr. Jack Hansen   1

3. Commanding Officer
    Naval Air Propulsion Center
    Trenton, NJ 08628
    Attention: G. Mangano, PE-31   1

4. Commanding Officer   1
    Naval Air Development Center
    Warminster, PA 19112
    Attention: AVTD

5. Library   1
    Army Aviation Material Laboratories
    Department of the Army
    Fort Eustis, VA 23604

6. Dr. Arthur J. Wennerstrom   1
    AFWAL/POTX
    Wright-Patterson AFB
    Dayton, OH 45433

7. Air Force Office of Scientific Research   1
    AFOSR/NA
    Bolling Air Force Base
    Washington, DC 20332
    Attention: Dr. James Wilson

8. National Aeronautics & Space Administration
    Lewis Research Center
    21000 Brookpark Road
    Cleveland, OH 44135
    Attention: Chief, Internal Fluid Mechanics Division   1
                Library   1
                N. Sanger   MS 5-11   1
                J. Adamcyzk   MS 5-11   1
                R. Chima   MS 5-11   1
                P. Sockol   MS 5-11   1
                J. Sanz   MS 5-11   1

09. Library   1
    General Electric Company
    Aircraft Engine Technology Division
    DTO Mail Drop H43
    Cincinnati, OH 45215

10. Library   1
    Pratt & Whitney Aircraft Group
    Post Office Box 2691
    West Palm Beach, FL 33402

11. Library   1
    Pratt-Whitney Aircraft Group
    East Hartford, CT 06108

12. Library   1
    Curtis Wright Corporation
    Woodridge, NJ 07075

13. Library   1
    AVCO/Lycoming
    550 S. Main Street
    Stratford, CT 06497

14. Library   1
    Teledyne CAE, Turbine Engines
    1330 Laskey Road
    Toledo, OH 43612

15. Library   1
    Williams International
    P. O. Box 200
    Walled Lake, MI 48088

16. Allison Gas Turbine Division   1
    General Motors Corporation
    P.O. Box 420
    Indianapolis, IN 46206-0420
    Attention: Dr. R.A. Delaney

17. Library   1
    Garrett Turbine Engine Company
    111 S. 34th Street
    P. O. Box 5217
    Phoenix, AZ 85010

18. Professor J. P. Gostelow   1
    School of Mechanical Engineering
    The New South Wales Institute of Technology
    New South Wales
    AUSTRALIA

19. Dr. G. J. Walker   1
    Civil and Mechanical Engineering
      Department
    The University of Tasmania
    Box 252C
    GPO Hobart, Tasmania 7110
    AUSTRALIA

20. Professor F. A. E. Breugelmans   1
    Institut von Karman de la Dynamique
      des Fluides
    72 Chausee de Waterloo
    1640 Rhode-St. Genese
    BELGIUM

21. Professor Ch. Hirsch   1
    Vrije Universiteit Brussel
    Pleinlaan 2
    1050 Brussels
    BELGIUM

22. National Aeronautics & Space Administration
    AMES Research Center
    Moffett Field, CA 94035
    Attention: Dr. Man M. Rai   (RFA:258-D)   1
               Dr. Paul Kutler (RFA:258-D)   1

23. Dr. John Denton   1
    Whittle Laboratory
    Department of Engineering
    Cambridge University
    ENGLAND

24. Library   1
    ONERA
    29, Ave. de la Division Leclerc
    92 Chatillon
    FRANCE

25. Professor D. Adler   1
    Technion Israel Institute of Technology
    Department of Mechanical Engineering
    Haifa 32000
    ISRAEL

26. Dr. P. A. Paranjpe   ^   1
    Head, Propulsion Division
    National Aeronautics Laboratory
    Post Bag 1700
    Bangalore - 17
    INDIA

27. Dr. W. Schlachter   1
    Brown, Boveri Company Ltd.
    Dept. T-T
    P. O. Box CH-5401 <u>Baden</u>
    SWITZERLAND

28. Professor Leonhard Fottner   1
    Department of Aeronautics and Astronautics
    German Armed Forces University
    Hochschule des Bundeswehr
    Werner Heisenbergweg 39
    8014 Neubiberg near Munich
    WEST GERMANY

29. Professor Dr. Ing. Heinz E. Gallus   1
    Lehrstuhl und Institut feur Strahlantiebe
     und Turbourbeitsmashinen
    Rhein.-Westf. Techn. Hochschule Aachen
    Templergraben 55
    5100 Aachen
    WEST GERMANY

30. Dr. Ing. Hans-J. Heinemann   1
    DFVLR-AVA
    Bunsenstrasse 10
    3400 Geottingen
    WEST GERMANY

31. Dr. H. Weyer   1
    DFVLR
    Linder Hohe
    505 Porz-Wahn
    WEST GERMANY

32. United Technologies Research Center
    East Hartford, CT 06108
    Attention: Dr. R.P. Dring   1
               Dr. J. Verdon   1
               Dr. R.L. Davis   1
               Dr. J.E. Carter   1

33. Director, Gas Turbine Laboratory   1
    Aeronautics and Astronautics Department
    31-265 Massachusetts Institute of Technology
    Cambridge, Massachusetts 02139

34. Dr. B. Lakshminarayana   1
    Professor of Aerospace Engineering
    The Pennsylvania State University
    233 Hammond Building
    University Park, Pennsylvania 16802

35. Mr. R. A. Langworthy   1
     Army Aviation Material Laboratories
     Department of the Army
     Fort Eustis, VA 23604

36. Mechanical Engineering Department
     Virginia Polytechnic Institute and
         State University
     Blacksburg, VA 24061
     Attention: Professor W. O'Brian   1
                 Professor H. Moses   1
                 Professor J. Moore   1

37. Professor T. H. Okiishi   1
     Professor of Mechanical Engineering
     208 Mechanical Engineering Building
     Iowa State University
     Ames, Iowa 50011

38. Dr. Fernando Sisto   1
     Professor and Head of Mechanical
         Engineering Department
     Stevens Institute of Technology
     Castle Point
     Hoboken, NJ 07030

39. Dr. Leroy H. Smith, Jr.   1
     Manager, Compressor and Fan
         Technology Operation
     General Electric Company
     Aircraft Engine Technology Division
     DTO Mail Drop H43
     Cincinnati, OH 45215

40. Dr. W. Tabakoff   1
     Professor, Department of Aerospace
         Engineering
     University of Cincinnati
     Cincinnati, OH 45221

41. Mr. P. Tramm   1
     Manager, Research Labs
     Detroit Diesel Allison Division
     Genteral Motors
     P. O. Box 894
     Indianapolis, IN 46206

42. Mr. P. F. Yaggy   1
     Director
     U. S. Army Aeronautical Research Laboratory
     AMES Research Center
     Moffett Field, CA 94035

43. Defense Technical Information Center   2
    Cameron Station
    Alexandria, VA   22314

44. Naval Postgraduate School
    Monterey, CA   93943-5100
    Attention: Professor M. F. Platzer (67Pl)   1
               Turbopropulsion Laboratory (67Sf)   15
               Library (1424)   2
               Research administration (012)   1

45. Dr. August Verhoff   30
    McDonnell Aircraft Company
    Mail Code: 341/32/2/MS122
    P.O. Box 516
    St. Louis, MO 63166

46. Dr. Steven Shamroth   1
    Scientific Research Associates
    P.O. Box 498
    Glastonbury, CT 06033

47. Dr. Chunill Hah   1
    General Electric Company
    CR & D K-1
    Schenectady, NY 12345